ACS Photonics

pubs.acs.org/journal/apchd5

Article

Laminar Flow-Optimized Confined Geometry Assistant Solution Growth of Large-Sized $CsPbBr_3$ Single Crystals for High-Sensitivity X-ray Detection

Ruichen Bai, Xin Liu,*,⊥ Zihang Lin, Siliang Hu, Xin Zhang, Johnny C. Ho, Rongrong Guo, Wanqi Jie, and Yadong Xu*,⊥

Cite This: https://doi.org/10.1021/acsphotonics.5c01079

Read Online

ACCESS | Metrics & More | Article Recommendations | Supporting Information

ABSTRACT: The $CsPbBr_3$ crystal grown by the solution method is regarded as an attractive and cost-effective material for radiation detection. However, approaching large-size, high-quality $CsPbBr_3$ single crystals is restricted by mass nucleation and an unstable growth interface. Here, the confined geometry assisted solution method is employed to obtain high-quality $CsPbBr_3$ single crystals with dimensions up to 17 × 17 × 2 mm^3. High yield growth of $CsPbBr_3$ seed crystals is achieved by adopting 2-bromopropionic acid (2-BPA) in the precursor, which expands the metastable zone twice and reduces nucleation. The crystal growth environment, simulated with a specific laminar flow model, reveals the uniform concentration distribution is realized by suitable forced convection velocity, thereby substantially enhancing the stability of the crystal growth interface. The resulting $CsPbBr_3$ single crystal exhibits low trap density states of 2.27 × 10^9 cm^{-3}, leading to a high hole mobility of 377.63 cm^2 V^{-1} s^{-1}. Finally, a high sensitivity of 1.6 × 10^5 μC Gy_{air}^{-1} cm^{-2} is realized under 50 kVp X-rays at 500 V cm^{-1}. These results promote the application of large-sized $CsPbBr_3$ single crystals in X-ray radiation detection as well as the reference and guidance for the growth of other perovskite single crystals.

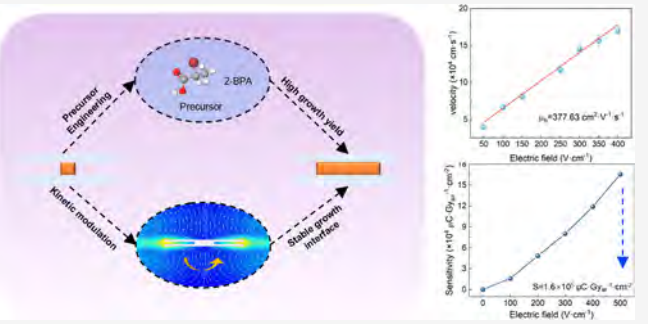

KEYWORDS: *$CsPbBr_3$, single crystal, solution growth, precursor engineering, kinetic modulation, radiation detection*

INTRODUCTION

Large-sized and highly sensitive X-/γ-ray radiation detectors are conducive for a wide range of industrial and biomedical applications.[1,2] Inorganic lead halide perovskite $CsPbBr_3$ single crystal (CPB SC) has recently shown great promise as a next-generation radiation detector due to its outstanding optoelectronic properties.[3−6] Nowadays, the cost-efficient synthesis of detector-grade CPB SCs through the solution method greatly facilitates their commercialization.[5,7] However, the reported solution-grown CPB SC size was limited due to mass nucleation in the precursor,[6,8] which is unfavorable to X-/γ-ray spectroscopy and imaging applications.[9,10] Furthermore, there is an intense demand for large-sized crystals with superior carrier transport behavior, but this is restricted by crystal defects, which are ascribed to the unstable growth interface.[11,12] Therefore, for scalable device production, the synthesis of large-sized, high-quality CPB SC through a solution method has been a major challenge.

At present, the introduction of seed crystals in the precursor is employed to grow large-sized perovskite single crystals.[8,13,14] However, the low growth yield (less than 5%[15]) caused by multiple nucleation limits the size of CPB SCs. It is known that the nucleation rate (j_0) in the solution is determined by the temperature (T) and supersaturation (σ), which is proportional to actual concentration minus solubility.[16,17]

$$j_0 \propto \exp\left(-\frac{1}{\sigma^2 T}\right) \tag{1}$$

As regulating temperature or supersaturation is the way to reduce the nucleation rate, some precursor engineering strategies have been proposed in previous studies.[18−21] By using a mixture of dimethyl sulfoxide (DMSO) with dimethylformamide (DMF) and cyclohexanol (CyOH), the crystal nucleation and growth temperature can be significantly reduced from over 100 to 25 °C−75 °C. However, multiple nuclei and polycrystallinity still occurred.[18] Therefore, tailoring the supersaturation to adjust the width of the metastable region where the nucleation is close to zero is considered to be a more effective way. The solubility of CsBr was enhanced to

Received: May 14, 2025
Revised: August 8, 2025
Accepted: August 11, 2025

decrease supersaturation by using ethylene glycol (EG), but $PbBr_2$ was poorly soluble in EG and, in turn, easily formed Cs_4PbBr_6.[19] Moreover, the $PbBr_2$·2DMSO and $PbBr_2$·2DMSO·glyoxylic acid (GLA) were found to lower the rate of $[PbBr_x]^{2-x}$ release, thereby expanding the metastable zone and reducing nucleation.[20,21] Consequently, the ability to expand the metastable zone through precursor engineering is considered an effective way to produce large-sized crystals.

The seed growth method is essentially an epitaxial method; the defects and impurities on the surface of the seed crystals tend to result in the propagation of dislocations and point defects.[22] In addition, since the solute concentration decreases as the crystal grows, inefficient solute transport leads to an unstable growth interface and structural defects.[23] Yan et al.[24] and Wang et al.[25] revealed that the heterogeneity of surface concentration distribution is a key factor affecting the growth interface stability and formation of liquid inclusion defects. It has been demonstrated that while the kinetic modulation via forced convection ensures the uniformity of solute supply to the growth interface,[26,27] unfavorable convection conditions usually cause undesirable surface concentration distribution, thereby degenerating the crystal quality.[28,29] Therefore, numerical simulation is preferable to visualize the flow and mass transport occurring in the seed solution method to assist crystal growth. Wang et al.[26] and Liu et al.[30] used numerical simulation to indicate that the high-quality potassium dihydrogen phosphate (KDP) and ammonium dihydrogen phosphate (ADP) crystals could be grown at the suitable rotation rate range by promoting surface supersaturation and uniformity with supersaturation variations at the surface below 2.3 and 2%, respectively. However, different from the flow field of KDP and ADP crystal growth that belongs to turbulence, the simulation of CPB SC growth with laminar flow and complex solvent compositions has not been explored so far. Therefore, the specific model must be designed to reflect the concentration distribution and flow field during CPB crystal growth.

In this work, we report the large-sized CPB SC grown by the confined geometry growth method (CGGM), which is combined with precursor engineering and kinetic modulation. The seed crystal growth yield is improved to 32% by tailoring the precursor solution with a 2-bromopropionic acid (2-BPA) additive. A stable solid−liquid interface is achieved by introducing forced convection, in which the parameters are optimized by the multiphysics simulation. Accordingly, we synthesized the $CsPbBr_3$ crystal with a size of 17 × 17 × 2 mm^3, which realizes the sensitivity of 1.6 × 10^5 $\mu C\ Gy_{air}^{-1}\ cm^{-2}$ under X-rays.

EXPERIMENTAL SECTION

Crystal Preparation. The seed crystals were first prepared by dissolving 12.5 mmol of CsBr (≥99.9%, Aladdin) together with 25 mmol of $PbBr_2$ in 25 mL of DMSO (≥99.5%, Aladdin). Subsequently, 16 mL of DMF and 9 mL of CyOH were added to create the precursor solution. The mixture was placed in a water bath and gradually started heating from 40 °C and then stopped heating until an ∼3 × 3 × 2 mm^3 $CsPbBr_3$ seed crystal was obtained. For crystals grown by the free growth method (FGM), 50 mmol of CsBr together with 100 mmol of $PbBr_2$ and 1 g of bromoacetic acid were dissolved in 100 mL of DMSO with continuous stirring for 6 h at room temperature. Immediately after, the solution was filtered using a membrane with a pore size of 0.2 μm. Then, a 100 mL mixture of DMF and CyOH was poured into the filtered solution to prepare precursors. Subsequently, the precursor was poured into the growth container, where a $CsPbBr_3$ seed crystal of 3 × 3 × 2 mm^3 was placed on the growth platform that was connected to a rotary motor. After that, the growth platform was transferred to a growth container. As the quality of the crystal grown along the [202] orientation is much better than that along the [040] orientation (Figure S1), all the epitaxial crystals were grown using [202] orientation seed crystals. Then, the temperature was decreased to 35 °C for Ostwald ripening, followed by heating from 40 to 50 °C with the platform rotating at speeds between 1 rpm and 10 rpm to obtain CPB SCs. In the case of crystals grown by CGGM, the steps for configuring the precursor solution are the same as in FGM. Then, the precursor was put in the growth container, and a 3 × 3 × 2 mm^3 $CsPbBr_3$ seed crystal was placed between quartz slices with a spacing of 2 mm placed on the growth platform, which was contacted with a rotary motor. Subsequently, the growth container was placed in a water bath and decreased to 35 °C for Ostwald ripening, followed by heating from 40 to 50 °C with the platform rotating at speeds between 1 rpm and 10 rpm to obtain CPB SCs.

Simulation Detail. COMSOL Multiphysics was used to carry out the concentration and flow field simulation. The laminar flow was used to define the flow field distribution, and the dilute substance transfer was used to define the concentration gradients near the CPB crystal surfaces. The coupling of laminar flow and dilute matter transfer was carried out by using a reaction flow and dilute matter physical field. A stirrer module was also used to simulate the rotation of the seed rod in the container to introduce forced convection. A three-dimensional geometric model was created according to the real crystal growth container, which contains the growth container, precursor solution, glass platform, and the CPB crystal (the size of CPB is 10 × 10 × 2 mm^3), as shown in Figure S2.

Characterization and Measurement. The XRD pattern was collected using the D/Max2500PC with Cu $K_{\alpha 1}$ in the range of 5−80° (2θ). The tube voltage and current were 40 kV and 40 mA, respectively. The DX-9BJ X-ray crystal orientation instrument was used to examine the double-crystal X-ray diffraction rocking curves with a tube current of 0.2 mA and a scan step of 1″. The morphology of the CPB crystal was analyzed by using a JSM-7500F field emission scanning electron microscope. A Nikon ECLIPSE LV100ND optical microscope was utilized to observe in situ the growth process of the CPB seed crystal. The steady-state photoluminescence spectra were tested with a Horiba Fluorolog FL-3. The transient photoluminescence (TRPL) spectrum was obtained using a modular fluorescence lifetime system (DeltaFlex).

α-Particle Detection Measurement. First, the 1.76 mm^2 round Au electrodes were configured in a parallel-plate geometry without a guard ring. The current−voltage (I−V) characteristic curve was obtained using an electrical properties measurement device (Agilent 4155C). The charge carrier mobility was determined using the time-of-flight (TOF) technique with a ^{241}Am@5.5 MeV α-particle source. The pulse shape data was collected by connecting the preamplifier (ORTEC 142) and output to a high-speed waveform digitizer card. The amplifier (ORTEC570) amplified and shaped the signals from the preamplifier. Finally, the pulse height spectra were obtained by using a conventional multichannel analyzer (ORTEC Easy-MCA).

https://doi.org/10.1021/acsphotonics.5c01079
ACS Photonics XXXX, XXX, XXX−XXX

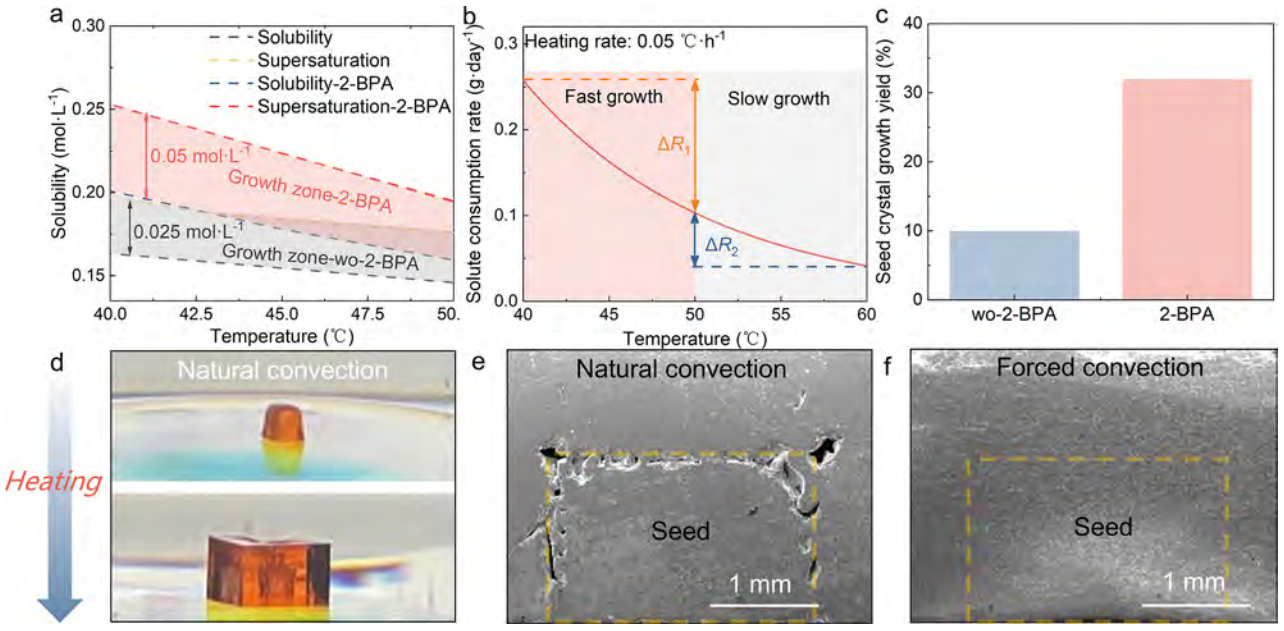

Figure 1. (a) The metastable zone of the precursor with the 2-BPA additive and without 2-BPA. (b) The solute consumption rate with a heating rate of 0.5 °C day^{-1}. (c) The yield of $CsPbBr_3$ seed crystals grown with and without 2-BPA. (d) The picture of a seed crystal grown after Ostwald ripening. The scanning electron microscopy (SEM) image of the crystal cross-section of a seed crystal grown under (e) natural convection and (f) forced convection.

X-ray Detection Measurement. A tungsten target X-ray tube was employed as the X-ray source. The Keithley 6517B provided the bias voltage and recorded the response current. The tube voltage was set as 50 kV, and the tube current was tuned from 0.3 to 0.8 mA to adjust the emitted X-ray dose rate. In the X-ray imaging experiment, a simple point imaging system was used to evaluate its imaging capability. The X-ray tube and planar CPB detector were oriented horizontally. The imaging capacity of the CPB detector was tested by moving an object on an $x-y$ scanning system that measures the detector's response current related to the position of the object. The imaging items were moved point by point by a 3D-controlled moving stage. A Keithley 6517B was used to generate a 5 V mm^{-1} electric field and record detector current.

RESULTS AND DISCUSSION

The low solubility of CsBr in DMSO (0.5 mol L^{-1}) is an important factor hindering the growth of large-sized CPB SC. In our mixed solvent system of DMSO/DMF/CyOH, the solubility of CsBr is only 0.25 mol L^{-1} at room temperature. Figure 1a shows that the solubility and supersaturation curves divide the crystal growth region into three sections: unsaturated (lower than the solubility curve), supersaturated (higher than the supersaturation curve), and metastable (between the solubility and supersaturation curves) zones. Spontaneous nucleation occurs exclusively in the supersaturated zone. For seed-assisted growth conditions, maintaining crystal growth within the metastable zone prevents excessive nucleation, which is crucial for obtaining large-sized crystals. However, in the precursor without additive, which is called the wo-2-BPA, the width of the metastable zone is only 0.025 mol L^{-1}, significantly narrower than other perovskites, so that large-sized single crystals can be obtained, as shown in Table 1. It has been reported that the bromoacetic acid (BAA) can increase the solubility of CsBr;[20] in this work, 2-BPA and 3-BPA were added to the precursor. Our previous study

Table 1. Width of the Metastable Zone of Different Perovskite Crystals

	width of the growth zone (mol L^{-1})	reference
$FAPbBr_3$	0.1	32
$MAPbBr_3$	0.2	33
$MAPbI_3$	0.15	34
$CsPbBr_3$	0.025	this work—wo-2-BPA
$CsPbBr_3$	0.05	this work—2-BPA

indicated the nucleation could be seen at 40 °C;[11,31] therefore, the precursor was kept at 40 °C for 24 h. It can be seen in Figure S3a,b that with the addition of 2-BPA, the nucleation number is significantly lower compared to the precursors without the additive or with the 3-BPA additive. Therefore, the 2-BPA additive is selected to grow CPB SCs. As shown in Figure 1a, both the solubility and the supersaturation are increased with the 2-BPA additive because 2-BPA will first react with DMSO, producing Br^- and a compound, which will next decompose into pyruvic acid (PYA) and dimethyl sulfide. The expansion of the metastable zone is caused by the PYA connecting with $PbBr_2$ via Pb = O, which can slow the rate at which $[PbBr_n]^{2-n}$ participates in the reaction to create $CsPbBr_3$, resulting in less $CsPbBr_3$ precipitated at the same temperature (Figure S4), so that the metastable zone can be substantially expanded to 0.05 mol L^{-1}. The expansion of the growth zone makes it easier to regulate seed crystal growth progress and reduce redundant nucleation (Figure S3c).

In order to achieve the large-sized CPB SC, the solute consumption rate (R) should also be considered, as shown in eq 2:[13]

$$R = \frac{dm}{dt} = -\frac{1}{2}VM\frac{dC(T)}{dT}\frac{dT}{dt} \quad (2)$$

where m is the mass of the crystal in grams, C is the solution concentration, V is the solution volume, M is the molar weight

https://doi.org/10.1021/acsphotonics.5c01079
ACS Photonics XXXX, XXX, XXX−XXX

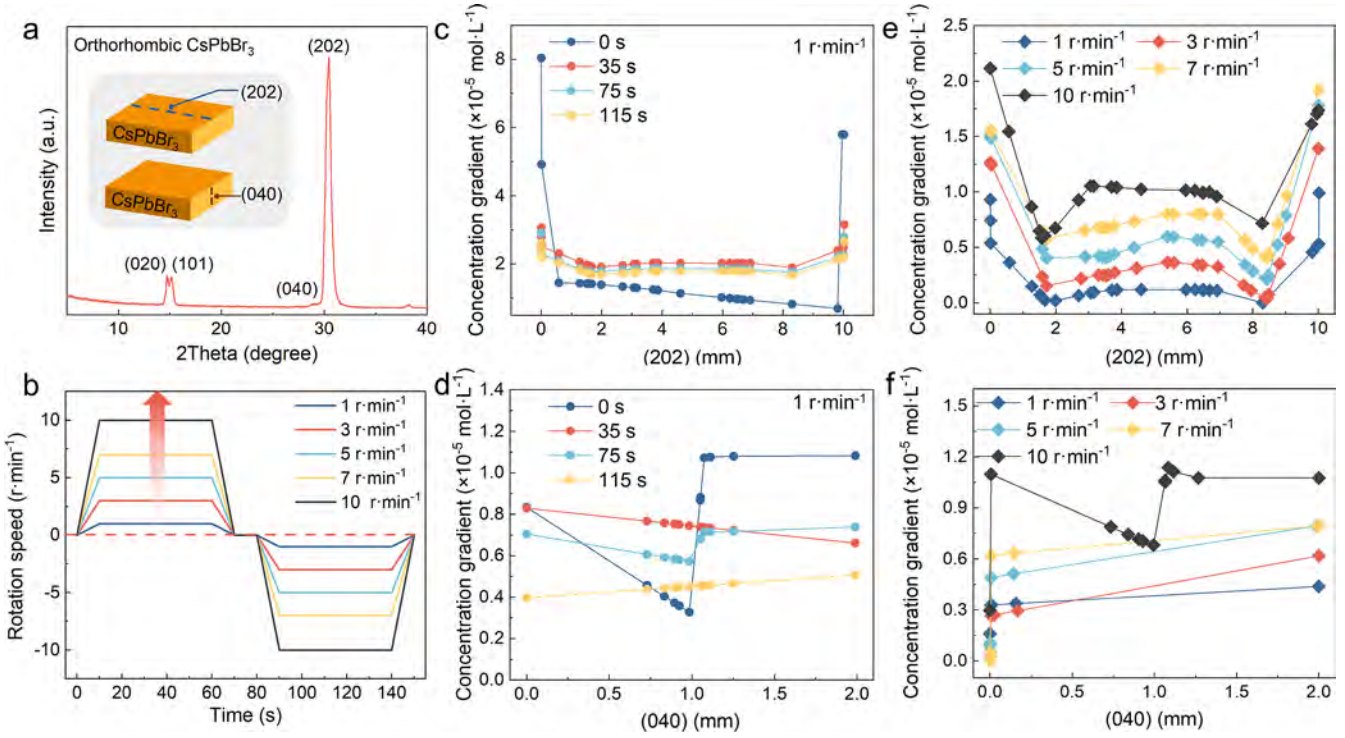

Figure 2. (a) The XRD pattern of CPB SCs. (b) The time-dependent rotation schedule that is adopted for $CsPbBr_3$ seed crystal growth. The concentration distribution at different times in the line segments on the (c) (202) surface and (d) (040) surface. The concentration distribution with different rotation speeds at 115 s in the line segments on the (e) (202) surface and (f) (040) surface.

of $CsPbBr_3$, T is the temperature, and t is the growth time. It can be seen that the solute consumption rate is proportional to both the temperature ramp rate and the first-order derivative of the concentration with the temperature, the latter of which can be calculated from the solubility curve. Figure 1b shows the solute consumption rate calculated using eq 2. It can be seen that ΔR is large in the low-temperature range (<50 °C), while ΔR changes little with temperature above 50 °C. Therefore, it takes a long time for CPB crystals to grow above 50 °C, and the growth temperature gradient is identified from 40 to 50 °C.

To indicate the difficulty of obtaining a large-sized single crystal, the seed crystal growth yield is defined in this work in eq 3:

$$Y = \frac{m_{\text{seed}}}{m_{\text{nucleation}} + m_{\text{seed}}} \tag{3}$$

where m_{seed} is the mass of seed crystal growth and $m_{\text{nucleation}}$ is the mass of the excess nucleation growth. The higher yield demonstrates less excess nucleation, resulting in the solutes being more enriched in the seed crystal and leading to large-sized CPB SCs. As shown in Figure 1c, the seed crystal grown with 2-BPA exhibits a 3 times higher yield (32%) than the wo-2-BPA crystal (10%), indicating that the addition of 2-BPA is an effective way to reduce excess nucleation.

During the seed growth process, as illustrated in Video S1, the steps and growth mounds on the seed crystal are first repaired before growth commences. As the rough surfaces and defects can degrade epitaxial crystal quality,[35] the Ostwald ripening (decreasing temperature to partially dissolve the seed crystal, followed by increasing temperature for growth) was employed. Figure 1d shows a CPB seed crystal grown with Ostwald ripening but reveals the interface that can gather dislocations and point defects. Because the forced convection introduced in crystal growth can make the surface supersaturation more uniform and guarantee stable step movement on the crystal surfaces,[36,37] the interfaces between the seed crystal and the epitaxial region in CPB SCs grown under natural convection and forced convection are compared. To ensure that the interface could be fully revealed, the crystals were separated in the middle and then corroded in 15% HBr acid for 10 min. The results indicate that under natural convection, a clear interface can be observed between the seed crystal and the epitaxial region (Figure 1e). Conversely, forced convection eliminates this interface (Figure 1f), as the deposition molecules take a longer time and a more stable step to settle in the correct crystal sites, reducing the number of structural defects. Therefore, forced convection is advantageous during the seed growth process.

To further reveal the effect of forced convection on the crystal growth interface, a finite element simulation of the concentration field for CPB seed crystal growth was carried out to aid in the design for the crystal growth method. The 3D model consists of a growth container and a crystal that is placed at the center of a rotating platform. Figure 2a illustrates the XRD pattern of CPB SC, which has two surfaces (202) and (040). Therefore, two lines are used to represent the concentration distribution on the center of the (202) and (040) surfaces, respectively. Figure 2b shows the time-dependent rotation schedule adopted for seed crystal growth, where alternating forward and backward rotations are used to promote the homogeneity of the precursor solution.

Figures 2c and 2d display the concentration gradient at the line segments on the (202) and (040) surfaces, respectively. The concentration gradient is defined as eq 4:

$$\Delta C = C_x - C_m \tag{4}$$

https://doi.org/10.1021/acsphotonics.5c01079
ACS Photonics XXXX, XXX, XXX−XXX

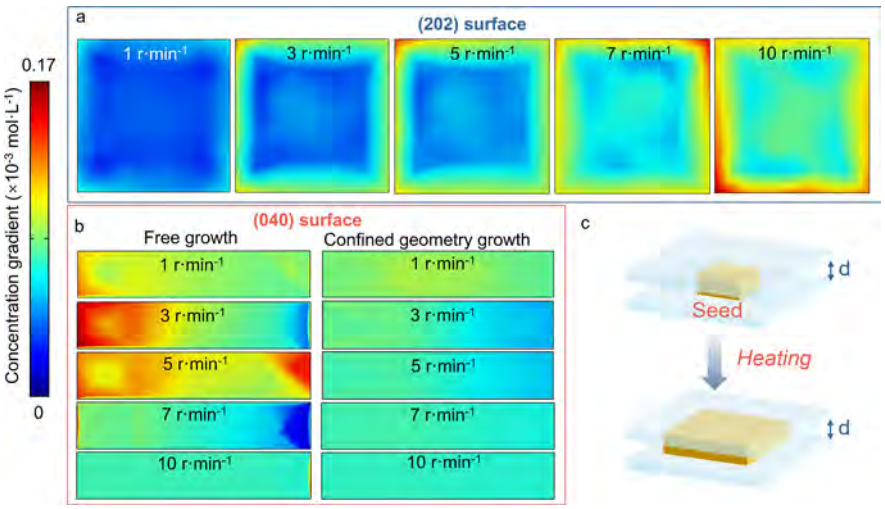

Figure 3. (a) The concentration distribution of the (202) surface in the FGM at 115 s. (b) The concentration distribution of the (040) surface in the situation of FGM and CGGM at 115 s, respectively. (c) The schema of CGGM.

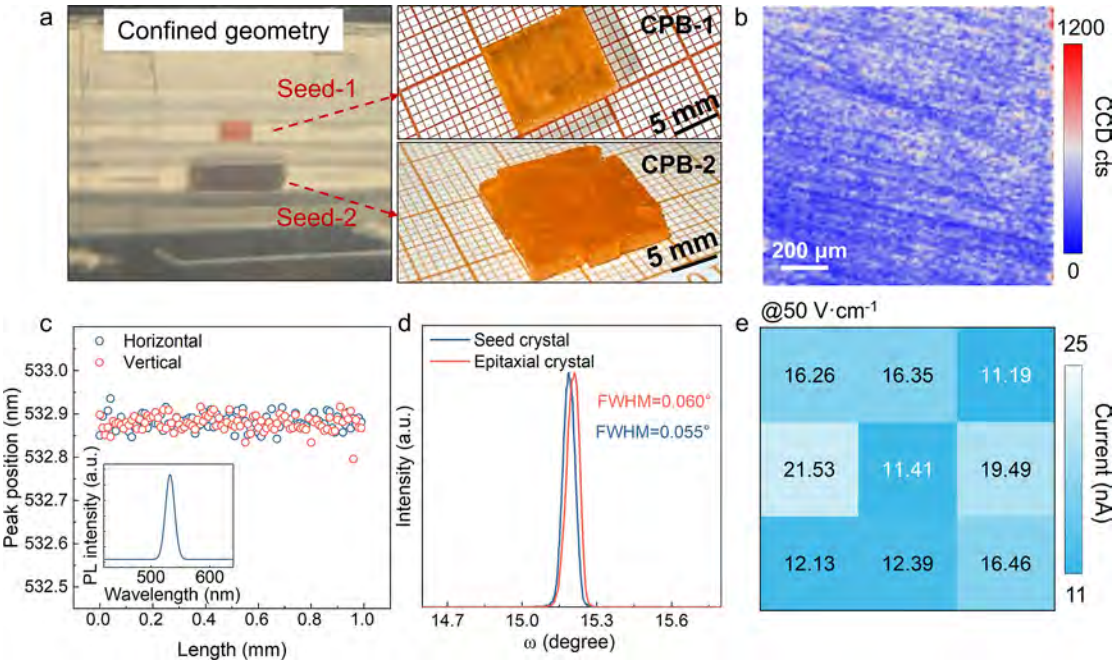

Figure 4. (a) The picture of the CGGM and the pictures of CPB SCs grown from Seed-1 and Seed-2. (b) The PL mapping of CPB-2. (c) The vertical projection at row $Y = 0.5$ mm and horizontal projection at column $X = 0.5$ mm at the indicated line; the inset is the PL spectrum from pixel A. (d) The X-ray rocking curve of the Seed-2 crystal and the epitaxial crystal grown by Seed-2. (e) The mapping of dark current at different regions on CPB-2.

where C_x is the concentration at location x and C_m is the minimum concentration on the line. It can be seen that once the platform begins to rotate, introducing forced convection, a more uniform concentration distribution on the crystal surface is achieved in both the forward (35 s) and reverse (115 s) rotation regions, even at the stopping time (75 s). The uniform concentration distribution weakens the "hunger center" phenomenon at the crystal growth interface, where higher concentration at the crystal edges results in the liquid being trapped in the crystal.[25] Such liquid inclusion defects can reduce crystal quality and deteriorate carrier transport behavior.[38] Thus, the forced convection promotes a more stable crystal growth interface and reduces structural defects, including liquid inclusion defects.

The concentration distribution with different rotation speeds at 115 s is also calculated as shown in Figures 2e and 2f. For both line segments, the uniform concentration distribution can be achieved at rotation speeds from 1 rpm to 10 rpm. Moreover, the concentration gets higher with higher rotation speed, which is due to the thinning of the crystal growth boundary layer. The boundary layer is caused by solute transport and deposition and creates a low concentration zone in front of the crystallization interface. Therefore, a higher rotation speed increases the shear rate at the crystal surface, reducing the thickness of the boundary layer, as shown in Figure S5, thus raising the concentration at the crystal surface.

To provide a comprehensive view of the homogeneity of the concentration distribution on the crystallization surface, a 2D

https://doi.org/10.1021/acsphotonics.5c01079
ACS Photonics XXXX, XXX, XXX−XXX

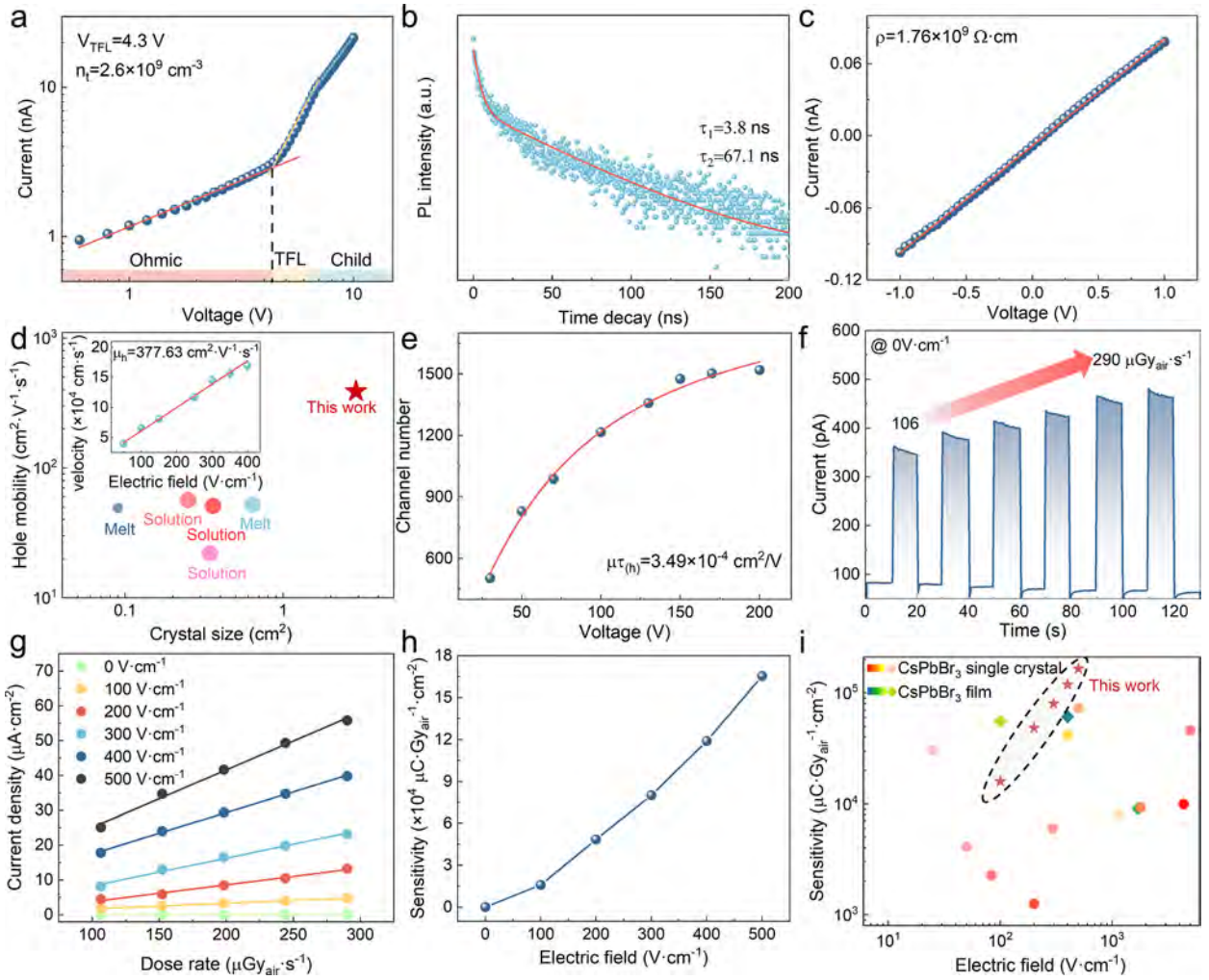

Figure 5. (a) The trap density of large-sized CPB SC according to the SCLC method. (b) The TRPL spectrum for the crystal at 533 nm. (c) The *I*−*V* curve of large-sized CPB SC from −1 to 1 V. (d) The hole mobility of large-sized CPB SC compared with CPB SCs grown in other works;[15,31,44−46] the inset is the hole mobility of CPB SC in this work. (e) The hole mobility−lifetime product of CPB SC is fitted by the Hecht equation. (f) Photocurrent of the CPB-2 planar device measured at different dose rates under X-ray radiation at 0 V bias. (g) The variation of current density with X-ray dose rate. (h) Sensitivity of the CPB-2 device under various biases. (i) Comparison of the X-ray response sensitivity of other $CsPbBr_3$ detectors.[5,6,20,41,47−56]

map distribution is shown in Figure 3. To meet the requirements of crystal thickness in radiation detection, which has been proven that 2 mm thick $CsPbBr_3$ can completely absorb 59.5 keV γ-rays,[39] as well as avoid mechanical damage caused by cutting, the confined geometry model was also constructed. Figure 3 shows the surface concentration distributions of both the CGGM and the free growth method (FGM).

The results indicate the low concentration area at the center of the (202) surface is visible with the rotation speed in the range of 1 rpm to 5 rpm. After the speed is higher than 7 rpm, the concentration distribution over the entire (202) surface is rather uniform and beneficial to obtain the stable crystal growth interface, which helps to obtain a high-quality CPB SC.

A comparison of the concentration distribution on the (040) surface of the FGM and CGGM can be seen in Figure 3b. Obviously, CGGM displays a more uniform concentration distribution. For the FGM, a stable crystal growth interface can only be achieved at a rotation speed of 10 rpm, which means the unstable surface with a lower rotation speed will trigger step bunching and increase the probability of inclusion formation.[25] However, the stable interface with concentration difference at the surface below 2 × 10^{-5} mol L^{-1} can be achieved when the rotation speed is higher than 5 rpm in the CGGM, which may be due to the elimination of the (202) surface effect on crystal growth. As the (202) surface has a growth boundary layer that causes a concentration gradient and natural convection, it may also affect the concentration distribution on the (040) surface. Therefore, the CGGM should be used as shown in Figure 3c. In addition, Figure S6 shows that a more stable average concentration can be obtained through CGGM. Moreover, the flow field of CGGM can be seen in Figure S7. It demonstrates that a rotation speed lower than 7 rpm causes a circular vortex cell in the confined space, which may hinder the solute transport in the confined space, resulting in the solute accumulation in the confined space and nucleation. Therefore, 7 rpm is a suitable rotation speed to grow CPB SCs.

According to the simulation results, the CGGM with a rotation speed of 7 rpm was used in the experiment to obtain large-sized CPB SC. Two seed crystals (Seed-1 and Seed-2) were used to grow large-sized crystals by this method as shown

https://doi.org/10.1021/acsphotonics.5c01079
ACS Photonics XXXX, XXX, XXX−XXX

in Figure 4a; the co-growth of multiple seed crystals is to increase the efficiency of obtaining crystals. The obtained crystals were named as CPB-1 and CPB-2, which exhibit large sizes of 12 × 10 × 2 mm^3 and 17 × 17 × 2 mm^3, respectively. The polarized optical microscopy images of CPB-2 are shown in Figure S8, which indicate that the crystal shows high quality and high uniformity. It is worth noting that the 17 × 17 × 2 mm^3 size CPB SC is the largest regular-shaped CPB SC obtained by the solution method.[5−7,15,18,20,40,41]

To confirm crystal uniformity, the mapping of photoluminescence (PL) intensity was measured using CPB-2 (Figure 4b), indicating the good surface uniformity of the large-sized crystal. As shown in Figures 4c and S9, the consistent PL peak position at different locations proves no other phases appear on the crystal surface, as the inset picture shows the typical PL peak of $CsPbBr_3$ is ∼533 nm (consistent with other literature[38,42]). In addition, as shown in Figure S10, no other phase appears in the $CsPbBr_3$ powder. To evaluate the epitaxial crystal quality, the X-ray rocking curve was also collected, and Figure 4d shows that the full width at half maxima (fwhm) of seed and epitaxial crystals is basically the same. However, the fwhm of crystals grown in FGM is much higher than that of CGGM, as shown in Figure S11. For single crystals, the fwhm broadening is mainly due to the angular rotation at dislocations.[34] Therefore, the result indicates that the stable growth interface facilitates the production of high-quality crystal while minimizing the generation of dislocations in the epitaxial crystal using the CGGM. Subsequently, the Au/$CsPbBr_3$/Au device was fabricated to test dark currents at different regions on CPB-2 under 50 V cm^{-1}. The results are shown in Figure 4e, and the measured dark currents map shows the difference below 10 nA. Such a low dark current would increase the detection capability of the detector under radiation and ensure the homogeneity of the radiation detector.

Since the stable growth interface can lead to fewer defects in the crystal and thus improve the carrier transport behavior, the defect density and carrier transport performance of CPB-2 were measured. First, the defect density state is determined using the space-charge-limited current (SCLC) technique that is shown in Figure 5a; the calculated trap density is 2.6 × 10^9 cm^{-3}, and the average trap density of the whole crystal calculated from Figure 4e is 2.27 × 10^9 cm^{-3} (Figure S12). The low trap density attests to the high quality of the large-sized crystals grown in this work. In addition, the time-resolved photoluminescence (TRPL) spectrum was collected to estimate the carrier lifetime τ, as shown in Figure 5b. CPB-2 shows a surface component (τ_1 = 3.8 ns) and a long bulk component (τ_2 = 67.1 ns). A longer τ suggests fewer nonradiative recombination centers (traps or defects) in the crystal, which demonstrates a lower trap-induced recombination rate in the crystal that is beneficial from the stable growth interface. Moreover, the lower trap density also helps to achieve the resistivity of 1.76 × 10^9 Ω cm (Figure 5c), which determines the operation bias voltage, leakage current noise, and, in turn, the radiation detection capacity of the device.

To evaluate the carrier transport performance of CPB-2, the Au/$CsPbBr_3$/Au devices' response to α particle by using the ^{241}Am@5.5 MeV source was tested to obtain the hole mobility (μ). The time-of-flight technique was adopted to evaluate the hole mobility of CPB SC, and the μ value was calculated to be 377.63 cm^2 V^{-1} s^{-1} (Figure S13), which is higher than the previous studies, as shown in Figure 5d. The high mobility due to the low trap density in the large-sized crystal is critical for the charge collection efficiency that dominates the sensitivity of the detectors. The pulse height spectrum of the device irradiated using a ^{241}Am@5.5 MeV source was measured as shown in Figure S14, and the hole mobility-lifetime product ($\mu\tau_{(h)}$) is fitted as 3.49 × 10^{-4} cm^2 V^{-1} (Figure 5e). The large $\mu\tau_{(h)}$ product is conducive to carrier collection and radiation detection signal perception.

Owing to the low defect density and excellent carrier transport properties of obtained CPB SC, the X-ray detection capability of CPB-2 was studied. Unlike the charged particle energy spectrum test conditions, X-ray response detection is based on the current mode. First, the asymmetric Sn/CPB-2/Au electrodes were formed to build the Schottky barrier to further decrease the dark current. Figure S15 shows the schematic diagram of the electrode structure, and the dark current at 100 V can be lower than 1 nA, which ensures the device's signal-to-noise ratio and stability during high-voltage detection. In addition, the built-in electric potential due to the Schottky barrier makes the device act as a self-driven detector operating without external energy. It can be seen in Figure 5f that, after eliminating the influence of gas ionization (Figure S16), the detector also shows an obvious response to X-rays under a 0 V bias. In addition, the X-ray response of the device from 100 V cm^{-1} to 500 V cm^{-1} is also measured, as shown in Figure S17. The linear relationship between current density and the X-ray dose rate represents the X-ray sensitivity (Figure 5g). Figure 5h shows the calculated sensitivity that can reach 165479.37 μC Gy_{air}^{-1} cm^{-2} under 500 V cm^{-1}. The optimal sensitivity of the detector is much higher than that of the commercial α-Se detector (20 μC Gy_{air}^{-1} cm^{-2})[43] and also higher than that of the other $CsPbBr_3$ detectors, as shown in Figure 5i. Moreover, it can be seen in Figure S18 that with high X-ray detection sensitivity and stable dark current, the $CsPbBr_3$ detector also achieves a high-resolution (1.0 LP mm^{-1}) X-ray image. The corresponding results indicate that the large-sized CPB SC grown by the CGGM has excellent application prospects for radiation detection.

CONCLUSION

In this work, the developed CGGM was explored to grow large-sized and high-quality CPB SC. First, the 2-BPA additive was employed to modify the precursor, for which the metastable zone was expanded twice and the growth yield increased from 10 to 32%. Whereafter, the finite element simulation was used to reveal the laws of forced convection velocity at crystal growth interfaces. A stable solid−liquid interface was obtained with the CGGM and a platform rotation speed of 7 rpm. Finally, the record large-sized CPB SC of 17 × 17 × 2 mm^3 was obtained, showing excellent homogeneity and low trap density of 2.27 × 10^9 cm^{-3}. The large-sized crystal exhibited high hole mobility (377.63 cm^2 V^{-1} s^{-1}) and excellent X-ray detection response with an X-ray sensitivity of 1.6 × 10^5 μC Gy_{air}^{-1} cm^{-2}, which also shows operational stability in a self-driven mode. Our work provides strategies for obtaining large-sized and high-quality CPB SCs, which can promote the further application of solution-grown $CsPbBr_3$ for radiation detection and hopefully stimulate and guide the growth technology of other large-sized perovskite single crystals for more applications.

https://doi.org/10.1021/acsphotonics.5c01079
ACS Photonics XXXX, XXX, XXX−XXX

■ ASSOCIATED CONTENT

Supporting Information

The Supporting Information is available free of charge at https://pubs.acs.org/doi/10.1021/acsphotonics.5c01079.

Detailed description of the simulation model, picture of $CsPbBr_3$ grown with an additive, PL mapping result, calculated trap density, X-ray detection results, and some experimental results of carrier transport behavior by the α particle (PDF)

Illustration of the seed growth process (MP4)

■ AUTHOR INFORMATION

Corresponding Authors

Xin Liu − *Aviation Engineering School, Air Force Engineering University, Xi'an 710038, China;* orcid.org/0000-0002-0409-1718; Email: liuxin8@mail.nwpu.edu.cn

Yadong Xu − *State Key Laboratory of Solidification Processing, and Key Laboratory of Radiation Detection Materials and Devices, Ministry of Industry and Information Technology, Northwestern Polytechnical University, Xi'an 710072, China;* orcid.org/0000-0002-1017-9337; Phone: +86-29-88460445; Email: xyd220@nwpu.edu.cn; Fax: 86-29-88495414

Authors

Ruichen Bai − *State Key Laboratory of Solidification Processing, and Key Laboratory of Radiation Detection Materials and Devices, Ministry of Industry and Information Technology, Northwestern Polytechnical University, Xi'an 710072, China*

Zihang Lin − *School of Optoelectronics and Communication Engineering, Xiamen University of Technology, Xiamen 361021, China*

Siliang Hu − *Department of Materials Science and Engineering, City University of Hong Kong, Kowloon, Hong Kong SAR 999077, China*

Xin Zhang − *State Key Laboratory of Solidification Processing, and Key Laboratory of Radiation Detection Materials and Devices, Ministry of Industry and Information Technology, Northwestern Polytechnical University, Xi'an 710072, China*

Johnny C. Ho − *Department of Materials Science and Engineering, City University of Hong Kong, Kowloon, Hong Kong SAR 999077, China;* orcid.org/0000-0003-3000-8794

Rongrong Guo − *School of Optoelectronics and Communication Engineering, Xiamen University of Technology, Xiamen 361021, China*

Wanqi Jie − *State Key Laboratory of Solidification Processing, and Key Laboratory of Radiation Detection Materials and Devices, Ministry of Industry and Information Technology, Northwestern Polytechnical University, Xi'an 710072, China*

Complete contact information is available at: https://pubs.acs.org/10.1021/acsphotonics.5c01079

Author Contributions

[⊥]X.L. and Y.X. contributed equally. The manuscript was written through contributions of all authors. All authors have given approval to the final version of the manuscript.

Funding

This work was supported by the National Key Research and Development Program of China (2023YFE0206300). This work was also supported by the National Natural Science Foundations of China (Nos. 12435013 and 52402018), the Natural Science Basic Research Plan in Shaanxi Province of China (2021GXLH-01-03 and 2024RS-CXTD-62), the ND Basic Research Funds (G2022WD), and the Young Talent Fund of Xi'an Association for Science and Technology (0959202513219).

Notes

The authors declare no competing financial interest.

■ REFERENCES

(1) Schlesinger, T. E.; Toney, J. E.; Yoon, H.; Lee, E. Y.; Brunett, B. A.; Franks, L.; James, R. B. Cadmium zinc telluride and its use as a nuclear radiation detector material. *Mater. Sci. Eng. R Rep.* **2001**, *32*, 103−189.

(2) Liu, F.; Chen, K.; Xue, D. How to fast grow large-size crystals? *Innovation* **2023**, *4*, 100458.

(3) Stoumpos, C. C.; Malliakas, C. D.; Peters, J. A.; Liu, Z.; Sebastian, M.; Im, J.; Chasapis, T. C.; Wibowo, A. C.; Chung, D. Y.; Freeman, A. J.; Wessels, B. W.; Kanatzidis, M. G. Crystal Growth of the Perovskite Semiconductor $CsPbBr_3$: A New Material for High-Energy Radiation Detection. *Cryst. Growth Des.* **2013**, *13* (7), 2722−2727.

(4) Zhang, M.; Zheng, Z.; Fu, Q.; Chen, Z.; He, J.; Zhang, S.; Chen, C.; Luo, W. Synthesis and single crystal growth of perovskite semiconductor $CsPbBr_3$. *J. Cryst. Growth* **2018**, *484*, 37−42.

(5) Zhang, H.; Wang, F.; Lu, Y.; Sun, Q.; Xu, Y.; Zhang, B.-B.; Jie, W.; Kanatzidis, M. G. High-sensitivity X-ray detectors based on solution-grown caesium lead bromide single crystals. *J. Mater. Chem. C* **2020**, *8*, 1248−1256.

(6) Pan, L.; Liu, Z.; Welton, C.; Klepov, V. V.; Peters, J. A.; De Siena, M. C.; Benadia, A.; Pandey, I.; Miceli, A.; Chung, D. Y.; Reddy, G. N. M.; Wessels, B. W.; Kanatzidis, M. G. Ultrahigh-Flux X-ray Detection by a Solution-Grown Perovskite $CsPbBr_3$ Single-Crystal Semiconductor Detector. *Adv. Mater.* **2023**, *35*, 2211840.

(7) Han, D.; Yang, K.; Bai, C.; Chen, F.; Sun, Z.; Wang, Y.; Ji, H.; Yang, Z.; Tang, X. Thermal and chemical durability of metal halide perovskite $CsPbBr_3$ single crystals. *Chem. Eng. J.* **2023**, *475*, 146209.

(8) Zhao, L.; Zhou, Y.; Shi, Z.; Ni, Z.; Wang, M.; Liu, Y.; Huang, J. High-yield growth of $FACsPbBr_3$ single crystals with low defect density from mixed solvents for gamma-ray spectroscopy. *Nat. Photonics* **2023**, *17*, 315.

(9) Liu, Y.; Zhang, Y.; Zhu, X.; Feng, J.; Spanopoulos, I.; Ke, W.; He, Y.; Ren, X.; Yang, Z.; Xiao, F.; Zhao, K.; Kanatzidis, M.; Liu, S. F. Triple-cation and mixed-halide perovskite single crystal for high-performance X-ray imaging. *Adv. Mater.* **2021**, *33*, 2006010.

(10) Bolke, J.; O'Brien, K.; Wall, P.; Spicer, M.; Gélinas, G.; Beaudry, J.-N.; Alexander, W. B. Measuring Te inclusion uniformity over large areas for CdTe/CZT imaging and spectrometry sensors. In *Proceedings Volume 10423, Sensors, Systems, and Next-Generation Satellites XXI*; SPIE, 2017..

(11) Bai, R.; Ge, B.; Liu, X.; Peng, X.; Zhang, X.; Liu, S.; Zhu, M.; Zhou, C.; Dubois, A.; Jie, W.; Xu, Y. Kinetic modulation-eliminated precursor liquid inclusions in solution-grown $CsPbBr_3$ bulk crystals for gamma-ray detection. *J. Mater. Chem. A* **2024**, *12*, 13925.

(12) Yang, T.; Jin, C.; Qu, J.; Darvish, A. A.; Sabatini, R.; Zhang, X.; Chen, H.; Ringer, S. P.; Lakhwani, G.; Li, F.; Cairney, J.; Liu, X.; Zheng, R. Solution Epitaxy of Halide Perovskite Thin Single Crystals for Stable Transistors. *ACS Appl. Mater. Interfaces* **2021**, *13*, 37840−37848.

(13) Liu, Y.; Zhang, Y.; Yang, Z.; Feng, J.; Xu, Z.; Li, Q.; Hu, M.; Ye, H.; Zhang, X.; Liu, M.; Zhao, K.; Liu, S. Low-temperature-gradient crystallization for multi-inch high-quality perovskite single crystals for record performance photodetectors. *Mater. Today* **2019**, *22*, 67−75.

(14) Liu, Y.; Yang, Z.; Cui, D.; Ren, X.; Sun, J.; Liu, X.; Zhang, J.; Wei, Q.; Fan, H.; Yu, F.; Zhang, X.; Zhao, C.; Liu, S. Two-Inch-Sized Perovskite $CH_3NH_3PbX_3$ (X = Cl, Br, I) Crystals: Growth and Characterization. *Adv. Mater.* **2015**, *27*, 5176−5183.

(15) Feng, Y.; Pan, L.; Wei, H.; Liu, Y.; Ni, Z.; Zhao, J.; Rudd, P. N.; Cao, L. R.; Huang, J. Low defects density $CsPbBr_3$ single crystals grown by an additive assisted method for gamma-ray detection. *J. Mater. Chem. C* **2020**, *8*, 11360−11368.
(16) Gibbs, J. W. On the equilibrium of heterogeneous substances. *Am. J. Sci.* **1878**, *s3−16* (16), 441−458.
(17) Bashkirov, A. G. A reconsideration of nucleation theory. *Phys. Lett. A* **1968**, *28*, 23−24.
(18) Dirin, D. N.; Cherniukh, I.; Yakunin, S.; Shynkarenko, Y.; Kovalenko, M. V. Solution-grown $CsPbBr_3$ perovskite single crystals for photon detection. *Chem. Mater.* **2016**, *28*, 8470−8474.
(19) Watanabe, S.; Hayashida, T.; Iwai, M.; Inomata, Y.; Kunitake, M.; Kida, T. Single Crystallization of Cs_4PbBr_6 Perovskite from Supersaturated Organic Solutions Optimized Through Solubility Studies. *ACS Omega* **2023**, *8*, 2455−2461.
(20) Xue, Z.; Wei, Y.; Li, H.; Peng, J.; Yao, F.; Liu, Y.; Wang, S.; Zhou, Q.; Lin, Q.; Wang, Z. Additive-Enhanced Crystallization of Inorganic Perovskite Single Crystals for High-Sensitivity X-Ray Detection. *Small* **2023**, *19*, 2207588.
(21) Yin, G.; Zhao, H.; Jiang, H.; Yuan, S.; Niu, T.; Zhao, K.; Liu, Z.; Liu, S. F. Precursor engineering for all-inorganic $CsPbI_2Br$ perovskite solar cells with 14.78% efficiency. *Adv. Funct. Mater.* **2018**, *28*, 1803269.
(22) Ye, F.; Lin, H.; Wu, H.; Zhu, L.; Huang, Z.; Ouyang, D.; Niu, G.; Choy, W. C. H. High-Quality Cuboid $CH_3NH_3PbI_3$ Single Crystals for High Performance X-Ray and Photon Detectors. *Adv. Funct. Mater.* **2019**, *29*, 1806984.
(23) Haruta, Y.; Ye, H.; Huber, P.; Sandor, N.; Pavesic Junior, A.; Dayneko, S.; Qiu, S.; Yeddu, V.; Saidaminov, M. I. Reproducible high-quality perovskite single crystals by flux-regulated crystallization with a feedback loop. *Nat. Synth.* **2024**, *3*, 1212.
(24) Yan, S.; Xie, C.; Zhang, X.; Zhou, L.; Hou, B.; Huang, J.; Zhou, L.; Yin, Q. Influence of crystal growth conditions on formation of macroscopic inclusions inside thiourea crystals. *Chem. Select* **2018**, *3*, 2293−2297.
(25) Wang, Y.; Zhang, N.; Hou, B.; Yin, Q.; Gong, J.; Tang, W. Effect of crystal growth kinetics on the formation of liquid inclusions in tetramethylpyrazine crystals. *CrystEngComm* **2020**, *22*, 1991−2001.
(26) Wang, P. F.; Li, M. W.; Liu, H. Numerical simulation of the hydrodynamics and mass transfer in the growth of KH_2PO_4 crystal through a frustum platform. *Int. J. Heat Mass Transfer* **2019**, *138*, 553−561.
(27) Ge, C.; Li, Y.; Song, H.; Xie, Q.; Zhang, L.; Ma, X.; Liu, J.; Guo, X.; Yan, Y.; Liu, D.; Zhang, W.; Liu, S.; Liu, Y. Anisotropic carrier dynamics and laser-fabricated luminescent patterns on oriented single-crystal perovskite wafers. *Nat. Commun.* **2024**, *15*, 914.
(28) Mischgofsky, F. H. Face stability and growth rate variations of the layer perovskite $(C_3H_7NH_3)_2CuCl_4$. *J. Cryst. Growth* **1978**, *44*, 223−234.
(29) Dinakaran, S.; Verma, S.; Jerome Das, S.; Kar, S.; Bartwal, K. S. Influence of forced convection on unidirectional growth of crystals. *Phys. Rev. B Condens. Matter* **2010**, *405*, 3919−3923.
(30) Liu, H.; Li, M. Numerical simulation of heat, mass and momentum transfer during $NH_4H_2PO_4$ crystal growth by solution circulating method. *J. Cryst. Growth* **2021**, *574*, 126343.
(31) Wang, F.; Bai, R.; Sun, Q.; Liu, X.; Cheng, Y.; Xi, S.; Zhang, B.; Zhu, M.; Jiang, S.; Jie, W.; Xu, Y. Precursor engineering for solution method-grown spectroscopy-grade $CsPbBr_3$ crystals with high energy resolution. *Chem. Mater.* **2022**, *34*, 3993−4000.
(32) Liu, X.; Zhang, Q.; Zhao, D.; Bai, R.; Ruan, Y.; Zhang, B.; Li, F.; Zhu, M.; Jie, W.; Xu, Y. Improved crystallization quality of $FAPbBr_3$ single crystals by a seeded solution method. *ACS Appl. Mater. Interfaces* **2022**, *14*, 51130−51136.
(33) Zhang, X.; Ji, C.; Liu, X.; Wang, S.; Li, L.; Peng, Y.; Yao, Y.; Hong, M.; Luo, J. Solution-Grown Large-Sized Single-Crystalline 2D/3D Perovskite Heterostructure for Self-Powered Photodetection. *Adv. Opt. Mater.* **2020**, *8*, 2000311.
(34) Wang, W.; Meng, H.; Qi, H.; Xu, H.; Du, W.; Yang, Y.; Yi, Y.; Jing, S.; Xu, S.; Hong, F.; Qin, J.; Huang, J.; Xu, Z.; Zhu, Y.; Xu, R.; Lai, J.; Xu, F.; Wang, L.; Zhu, J. Electronic-grade high-quality perovskite single crystals by a steady self-supply solution growth for high-performance X-ray detectors. *Adv. Mater.* **2020**, *32*, 2001540.
(35) Smalc-Koziorowska, J.; Kamler, G.; Łucznik, B.; Grzegory, I. Structural defects in GaN crystals grown by HVPE on needle-shaped GaN seeds obtained under high N_2 pressure. *J. Cryst. Growth* **2009**, *311*, 1407−1410.
(36) Zhu, Y.; Li, M.; Yin, H.; Wang, P.; Huang, J.; Liu, H. Growth and characterization of KDP crystals grown by the 2D-translation method equipped with continuous filtration. *Cryst. Growth Des.* **2020**, *20*, 3772−3779.
(37) Liu, X.; Zhang, Q.; Zhao, D.; Bai, R.; Hao, Y.; Fang, B.; Ruan, Y.; Zhang, B.; Wang, T.; Zhou, C.; Jie, W.; Xu, Y. Near-Net-Shaped Growth of Inch-Sized $MAPbBr_3$ Bulk Crystal by the Space-Confined Seeded Solution Method. *Cryst. Growth Des.* **2024**, *24*, 734−740.
(38) Musiienko, A.; Čížek, J.; Elhadidy, H.; Praus, P.; Higgins, K.; Dryzhakov, B.; Kanak, A.; Sureau, F.; Pipek, J.; Belas, E.; Betušiak, M.; Brynza, M.; Lukosi, E.; Hu, B.; Ahmadi, M. Origin of Defects and Positron Annihilation in Hybrid and All-Inorganic Perovskites. *Chem. Mater.* **2022**, *34*, 297−306.
(39) Zhang, X.; Li, F.; Bai, R.; Sun, Q.; Hao, Y.; Xi, S.; Zhu, M.; Jiang, S.; Jie, W.; Xu, Y. Investigation on energy resolution of $CsPbBr_3$ detectors: from charge transport behavior to device configuration. *J. Mater. Chem. C* **2022**, *10*, 6017−6024.
(40) Rakita, Y.; Kedem, N.; Gupta, S.; Sadhanala, A.; Kalchenko, V.; Böhm, M. L.; Kulbak, M.; Friend, R. H.; Cahen, D.; Hodes, G. Low-Temperature Solution-Grown $CsPbBr_3$ Single Crystals and Their Characterization. *Cryst. Growth Des.* **2016**, *16*, 5717−5725.
(41) Peng, J.; Xia, C. Q.; Xu, Y.; Li, R.; Cui, L.; Clegg, J. K.; Herz, L. M.; Johnston, M. B.; Lin, Q. Crystallization of $CsPbBr_3$ single crystals in water for X-ray detection. *Nat. Commun.* **2021**, *12*, 1531.
(42) Bechir, M. B.; Alresheedi, F. Growth methods' effect on the physical characteristics of $CsPbBr_3$ single crystal. *Phys. Chem. Chem. Phys.* **2024**, *26*, 1274−1283.
(43) Kasap, S. O. X-ray sensitivity of photoconductors: application to stabilized a-Se. *J. Phys. D: Appl. Phys.* **2000**, *33*, 2853.
(44) Pan, L.; Feng, Y.; Kandlakunta, P.; Huang, J.; Cao, L. R. Performance of perovskite $CsPbBr_3$ single crystal detector for gamma-ray detection. *IEEE Trans. Nucl. Sci.* **2020**, *67*, 443−449.
(45) He, Y.; Liu, Z.; McCall, K. M.; Lin, W.; Chung, D. Y.; Wessels, B. W.; Kanatzidis, M. G. Perovskite $CsPbBr_3$ single crystal detector for alpha-particle spectroscopy. *Nucl. Instrum. Meth. A* **2019**, *922*, 217−221.
(46) He, Y.; Petryk, M.; Liu, Z.; Chica, D. G.; Hadar, I.; Leak, C.; Ke, W.; Spanopoulos, I.; Lin, W.; Chung, D. Y.; Wessels, B. W.; He, Z.; Kanatzidis, M. G. $CsPbBr_3$ perovskite detectors with 1.4% energy resolution for high-energy γ-rays. *Nat. Photonics* **2021**, *15*, 36−42.
(47) Pan, W.; Yang, B.; Niu, G.; Xue, K.-H.; Du, X.; Yin, L.; Zhang, M.; Wu, H.; Miao, X.-S.; Tang, J. Hot-Pressed $CsPbBr_3$ Quasi-Monocrystalline Film for Sensitive Direct X-ray Detection. *Adv. Mater.* **2019**, *31*, 1904405.
(48) Du, X.; Liu, Y.; Pan, W.; Pang, J.; Zhu, J.; Zhao, S.; Chen, C.; Yu, Y.; Xiao, Z.; Niu, G.; Tang, J. Chemical Potential Diagram Guided Rational Tuning of Electrical Properties: A Case Study of $CsPbBr_3$ for X-ray Detection. *Adv. Mater.* **2022**, *34*, 2110252.
(49) Zhang, P.; Hua, Y.; Xu, Y.; Sun, Q.; Li, X.; Cui, F.; Liu, L.; Bi, Y.; Zhang, G.; Tao, X. Ultrasensitive and robust 120 keV hard X-Ray imaging detector based on mixed-halide perovskite $CsPbBr_{3-n}I_n$ single crystals. *Adv. Mater.* **2022**, *34*, 2106562.
(50) Hua, Y.; Zhang, G.; Sun, X.; Zhang, P.; Hao, Y.; Xu, Y.; Yang, Y.; Lin, Q.; Li, X.; Zhai, Z.; Cui, F.; Liu, H.; Liu, J.; Tao, X. Suppressed ion migration for high-performance X-ray detectors based on atmosphere-controlled EFG-grown perovskite $CsPbBr_3$ single crystals. *Nat. Photonics* **2024**, *18*, 870−877.
(51) Ren, Y.; Haruta, Y.; Dayneko, S.; Tao, J.; Zhang, D.; Yeddu, V.; Bazalova-Carter, M.; Saidaminov, M. I. Surface Chemistry of Solution-Grown $CsPbBr_3$ Single Crystals and Their Selective Cleaning for Linear-Responsive X-ray Detectors. *ACS Mater. Lett.* **2024**, *6*, 3763−3769.

https://doi.org/10.1021/acsphotonics.5c01079
ACS Photonics XXXX, XXX, XXX−XXX

(52) He, Y.; Hadar, I.; De Siena, M. C.; Klepov, V. V.; Pan, L.; Chung, D. Y.; Kanatzidis, M. G. Sensitivity and Detection Limit of Spectroscopic-Grade Perovskite $CsPbBr_3$ Crystal for Hard X-Ray Detection. *Adv. Funct. Mater.* **2022**, *32*, 2112925.
(53) Di, J.; Li, H.; Su, J.; Yuan, H.; Lin, Z.; Zhao, K.; Chang, J.; Hao, Y. Reveal the Humidity Effect on the Phase Pure $CsPbBr_3$ Single Crystals Formation at Room Temperature and Its Application for Ultrahigh Sensitive X-Ray Detector. *Adv. Sci.* **2022**, *9*, 2103482.
(54) Li, C.; Ye, X.; Jiang, J.; Guo, Q.; Zheng, X.; Lin, Q.; Ge, C.; Wang, S.; Chen, J.; Gao, Z.; Zhang, G.; Tao, X.; Liu, Y. High-Throughput Growth of Armored Perovskite Single Crystal Fibers for Pixelated Arrays. *Small* **2024**, *20*, 2401624.
(55) Wang, J.; Yu, S.; Jin, H.; Li, Y.; Zhang, K.; Phillips, D. L.; Yang, S. Nonstoichiometry Promoted Solventless Recrystallization of a Thick and Compact $CsPbBr_3$ Film for Real-Time Dynamic X-Ray Imaging. *Adv. Sci.* **2024**, *11*, 2407314.
(56) Zhao, X.; Wang, S.; Song, Y.; Aoki, T.; Gnatyuk, V.; You, L.; Deng, Z.; Tao, R.; Fang, X.; Meng, G. Freezing non-radiative recombination in high-performance $CsPbBr_3$ single crystal x-ray detector. *Appl. Phys. Lett.* **2024**, *125*, 083507.

https://doi.org/10.1021/acsphotonics.5c01079
ACS Photonics XXXX, XXX, XXX−XXX